AMERICAN METEOROLOGICAL SOCIETY
AMS Journals Online

Full Text View

Variability of the Thermocline Due to a Sudden Change in the Ekman Pumping

J. Sirven and C. Frankignoul

Laboratoire d'Océanographie Dynamique et de Climatologie, UMR: CNRS/ORSTOM/Université Pierre et Marie Curie, Paris, France

ABSTRACT

The thermocline variability caused by a sudden variation of the Ekman pumping is studied, using a 2.5-layer geostrophic model that represents the ventilated and the shadow zones of a subtropical gyre and baroclinic Rossby wave propagation. During spinup the propagation of the first baroclinic mode induces a large deepening of the thermocline on a timescale ranging between 2 and 15 yr, depending on latitude. The propagation is similar throughout the basin, and is not influenced by the geostrophic flow, save nonlinearly through the variation in layer depth. South of the subduction line, the adjustment is completed by the second baroclinic mode. In the ventilated zone, the latter is not very active, and there are only smaller (by a factor of 5) variations of the thermocline depth primarily linked to a slight imbalance between Ekman pumping and vertically averaged meridional advection. In the shadow zone, the second baroclinic mode plays a more important role since it primarily balances the Ekman pumping, although the variations of the second layer depth remain smaller than in the ventilated area. Spindown induces similarly a shoaling of the thermocline, but, because of nonlinearities, lower Rossby wave speeds, and decreased advection, the adjustment is everywhere slower than during spinup.

Options:
- Create Reference
- Email this Article
- Add to MyArchive
- Search AMS Glossary

Search CrossRef for:
- Articles Citing This Article

Search Google Scholar for:
- J. Sirven
- C. Frankignoul

1. Introduction

The observations show that the large-scale variability of the thermocline is small at the annual period (Frankignoul 1981) but substantial at low frequency. In the North Atlantic, for example, Joyce and Robbins (1996) described in-phase decadal changes of temperature and salinity in the thermocline near Bermuda that could be caused by vertical oscillations with a first baroclinic mode structure and amplitudes of ±50 m. Sturges and Hong (1995) analyzed the Bermuda tide gauge record and showed that the decadal variability was due to the (first mode) baroclinic response to wind stress forcing across the Atlantic, and Frankignoul et al. (1997, hereafter FMZ) suggested that it primarily reflected the thermocline response to the stochastic atmospheric forcing. Sturges et al. (1998) found that low frequency

wind forcing could explain the large decadal-scale thermocline fluctuations observed in the central North Atlantic. Experiments with coupled general circulation models (e.g., Latif and Barnett 1994; Zorita and Frankignoul 1997) also suggest that the decadal variabilitity of the midlatitude thermocline is largely wind driven.

Theoretical studies have shed some light onto the mechanisms of these decadal variations. Using a two-layer model of the ventilated thermocline, Liu (1993, hereafter Liu) suggested that the dynamics differ between the shadow zone, where Rossby waves balance the Ekman pumping and the variability is large, and the ventilated zone, where advection balances it and the variability is very weak. In a numerical study based on quasigeostrophic models, Liu (1996) suggested that the thermocline variability in the Rhines–Young pool (Rhines and Young 1982) is, as in the ventilated zone, dominated by advection and Ekman pumping, while Liu and Pedlosky (1994) found that, in contrast to wind stress forcing, buoyancy forcing causes a strong (weak) variability in the ventilated (shadow) zone. Although of much theoretical interest, these studies fail to explain how the atmosphere can force the first-mode-like thermocline variability, seen in the observations. On the other hand, simpler models that a priori specify a first baroclinic mode structure and assume a mean state at rest are more successful (Sturges and Hong 1995; FMZ). Thus, there is a need to link these studies and to establish which oversimplifications lead to such discrepancies.

For analytical simplicity, Liu had used a planetary geostrophic two-layer model with a rigid and flat bottom taken at the base of the main thermocline. This model allows fluid to subduct and so represents an essential feature of the ventilated thermocline, but the assumption of a flat thermocline is limiting. Moreover, with a zonal outcrop line, the model produces a uniform potential vorticity in the ventilated zone and thus prevents any planetary wave activity in this region. In the present paper, we generalize Liu's study of oceanic spinup and spindown to a more realistic 2.5-layer model, which does not impose a flat thermocline bottom and allows for nonuniform potential vorticity in the ventilated zone. It will be shown in particular that the largest part of the oceanic response to wind forcing is due to the first baroclinic mode, which was in effect filtered out by Liu and, to a coarse approximation, is not affected by the mean flow and thermocline stucture. This may explain in part the success of the simpler model of Sturges and Hong (1995), FMZ, and others.

The paper is arranged as follows. Section 2 describes the 2.5-layer model. In section 3, we discuss the solution north of the subduction line. In section 4 we solve the problem south of the subduction line and present the main results for the ventilated and shadow zones, emphasizing the role of the first baroclinic mode. In section 5, we define the second baroclinic mode and discuss its role in the return to equilibrium. Conclusions are given in section 6.

2. The model

We use a time-dependent version of a 2.5-layer ideal-fluid model of the ventilated thermocline derived from Luyten et al. (1983). Its geometry is shown in Fig. 1 ⚬. The eastern and western boundaries are at $x = 0$ and $x = x_w < 0$, and the geostrophic zonal flow vanishes at the eastern boundary ($h_1 = 0$ and $H = h_2 = H_0 = 500$ m). A downward Ekman pumping w_e is imposed at the surface and the subtropical gyre is limited by its vanishing at $y = y_N$ and $y = y_S$. The warmest layer of density ρ_1 and thickness h_1 is located south of y_1, where the second layer of density ρ_2 and thickness h_2 outcrops. The depth of the second layer $H = h_1 + h_2$ represents the base of the thermocline. The abyss is represented by a third layer of density ρ_3 at rest. It has an infinite depth to be consistent with the rigid lid, which is imposed at the surface. The β-plane approximation is used with Coriolis parameter $f = f_0 + \beta y$. The model is thus similar to that of Liu except that the base of the thermocline is allowed to vary and the barotropic mode is filtered out by the rigid-lid assumption. In each layer, the fluid is geostrophic:

$$\rho_n f u_n = -\frac{\partial p_n}{\partial y} \quad \text{and} \quad \rho_n f v_n = \frac{\partial p_n}{\partial x} \quad \text{with } n = 1, 2. \quad (1)$$

Hydrostatic equilibrium yields

$$\text{grad}_h p_1 = \rho_0 g(\gamma_1 \, \text{grad}_h h_1 + \gamma_2 \, \text{grad}_h H) \quad \text{and}$$

$$\text{grad}_h p_2 = \rho_0 g \gamma_2 \, \text{grad}_h H, \quad (2)$$

where $\text{grad}_h p$ is the horizontal pressure gradient, ρ_0 is a reference density, and $\gamma_1 = (\rho_2 - \rho_1)/\rho_0$ and $\gamma_2 = (\rho_3 - \rho_2)/\rho_0$ are both much smaller than 1 (Boussinesq approximation). The incompressibility condition is

$$\frac{\partial}{\partial x} \qquad \frac{\partial}{\partial y} \qquad \frac{\partial}{\partial z}$$

Replacing u_n and υ_n by (1) leads to $\beta \upsilon_n = f \partial_z w_n$, $n = 1, 2$ and, after integration from the top of the motionless layer to the surface, to the time-dependent Sverdrup relation:

$$\frac{\beta}{f}(h_1 \upsilon_1 + h_2 \upsilon_2) = w_e + \left(\frac{\partial}{\partial t} + u_2 \frac{\partial}{\partial x} + \upsilon_2 \frac{\partial}{\partial y}\right) H. \quad (4)$$

Since advection by the geostrophic velocity vanishes identically from (1) and (2), (4) can be simplified into

$$\frac{\beta}{f}(h_1 \upsilon_1 + h_2 \upsilon_2) = w_e + \frac{\partial H}{\partial t} \qquad (5)$$

or, using the Boussinesq approximation,

$$\frac{\partial H}{\partial t} - \frac{\beta g}{f^2}\left(\gamma_1 h_1 \frac{\partial h_1}{\partial x} + \gamma_2 H \frac{\partial H}{\partial x}\right) = -w_e. \qquad (6)$$

This relation also holds north of the subduction line, but with $h_1 = 0$, $h_2 = H$.

Integrating $\beta \upsilon_2 = f \partial_z w_2$ over the depth of the second layer south of the subduction line leads to the conservation of potential vorticity,

$$\left(\frac{\partial}{\partial t} + u_2 \frac{\partial}{\partial x} + \upsilon_2 \frac{\partial}{\partial y}\right)\frac{f}{h_2} = 0. \qquad (7)$$

Using (1), (2), and, once more, $|\rho_2 - \rho_0| \ll \rho_0$ leads to

$$\left(\frac{\partial}{\partial t} - \frac{g\gamma_2}{f}\frac{\partial H}{\partial y}\frac{\partial}{\partial x} + \frac{g\gamma_2}{f}\frac{\partial H}{\partial x}\frac{\partial}{\partial y}\right)\frac{f}{h_2} = 0, \qquad (8)$$

which, together with (6), describes the dynamics south of the subduction line.

For convenience, we use both the Coriolis parameter f and the latitude y as meridional coordinate. The Ekman pumping w_e is a parabolic function of latitude, $w_e = \alpha(t)(f_N - f)(f - f_S)$, which vanishes at $f_N = 10^{-4}$ s^{-1} (45°N) and $f_S = 1.3 \times 10^{-5}$ s^{-1} (5°N), thereby preventing a geostrophic transport at these latitudes. In the spinup case, we assume that at $t = 0$, $\alpha(t)$ instantaneously switches from $-2 \times 10^{-6}/(f_N - f_S)^2$ m s^{-1} to $-6 \times 10^{-6}/(f_N - f_S)^2$ m s^{-1} so that the maximum value of $|w_e|$ increases from 0.5×10^{-6} m s^{-1} to 1.5×10^{-6} m s^{-1}. The reverse is assumed during spindown. These wind stress changes are unrealistically large, but allow for an easy comparison with Liu, who used similar values. The outcrop line y_1 (or f_1) neither depends on x nor t and is located at $f_1 = 8.9 \times 10^{-5}$ s^{-1} (38°N); $\beta = 2.1 \times 10^{-11}$ m^{-1} s^{-1} corresponds to midbasin (25°N). Analytical computations are made with $\gamma_1 \neq \gamma_2$ but in the numerical experiments we use $\gamma_1 = \gamma_2 = 10^{-3}$.

3. Solution north of the subduction line

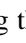In the steady state, (6) with $h_1 = 0$ can be integrated into

$$\beta\gamma_2(h_2^2 - H_0^2) = 2f^2 w_e x, \qquad (9)$$

where H_0 is the thermocline depth at the eastern side ($x = 0$). We assume that H_0 is known and choose for numerical

application $H_0 = 500$ m. When w_e varies, Rossby waves are generated, and (6) is solved by the method of characteristics; that is, it is replaced by the differential equations

$$dt = ds \qquad dx = c_R ds \quad \text{with } c_R = -\beta g \gamma_2 h_2 / f^2$$

$$dh_2 = -w_e ds, \qquad\qquad\qquad\qquad (10)$$

where s denotes abscissa along the characteristic and c_R is the phase speed of the first-mode baroclinic Rossby wave.

The condition at $s = 0$, indicated by subscript σ, is defined by prescribing the thermocline depth at $t = 0$ in the whole basin $[h_2 = h_{2\sigma}(x_\sigma, f)]$ and at $t > 0$ along the eastern boundary $(h_2 = H_0)$. Figure 2 , analytically computed from (10), shows the thermocline depth in its initial state, after 5 and 10 yr, and in the new steady state. The dashed line is the westward propagating wave front generated at the eastern boundary at $t = 0$. After the wave front has passed, the ocean reaches a new state of rest, and the subduction line is again at rest after 12 yr if the basin width is 6000 km. The spindown can be treated in the same way but is slower than the spinup because of the nonlinearities. The wave front moves more slowly (except along $y = y_N$ where w_e vanishes) and a new equilibrium is reached along the subduction line only after 15 yr.

Our results differ from those of Liu who found that the adjustment was only barotropic, hence instantaneous and without influence on the thermocline. This is due to Liu's assumption of a rigid thermocline bottom, which filters out the first baroclinic mode. A better approximation north of the subduction line would be to use a basic state at rest (e.g., FMZ) since advection by a geostrophic flow has no influence on the propagation of the first mode in the case where only one layer is active, save through the variation of layer depth. This non-Doppler shift effect holds for 1.5-layer models as shown by Anderson and Killworth (1979) (the two layer model they used assumes that the bottom layer is much deeper than the upper layer; thus its physics is the same that of the 1.5-layer model), but not in more general cases (e.g., Killworth et al. 1997). Note that we have assumed that H_0 was constant. However, a varying depth at the eastern side (for example due to coastal Kelvin waves) would lead to similar computations and results.

4. Solution south of the subduction line

South of the outcrop line $(f < f_1)$, in the initial (Fig. 3 , top) and final (bottom) states, the ventilated zone is easily distinguished from the shadow zone where the second-layer depth is constant, but the recirculation zone is not correctly represented since it obeys higher order dynamics (area limited by a dotted line). With a stronger Ekman pumping, the two upper layers are much deeper (by more than 150 m for layer 2) and the shadow zone narrower. In this section, we discuss the phenomena involved in this change, emphasizing the role of the first baroclinic mode and leaving that of the second to section 5.

To define the modes, we first change variables in (6) and (8). In a stationary state, integration of (6) yields

$$\frac{\gamma_1}{\gamma_2} h_1^2 + H^2 = \frac{2f^2}{\beta g \gamma_2} w_e x + H_0^2, \qquad\qquad (11)$$

which suggests using the variable (effective depth)

$$\mathcal{H} = \sqrt{\frac{\gamma_1}{\gamma_2} h_1^2 + H^2} \qquad\qquad (12)$$

to characterize the overall response of the thermocline to a variation in w_e. An increase of $\mathcal{H}$ corresponds to an increase of h_1 and/or h_2. From geostrophy, the averaged velocity $(u_a, \upsilon_a) = \mathbf{v}_a = (h_1 \mathbf{v}_1 + h_2 \mathbf{v}_2)/H$ is given by

$$H \mathbf{v}_a = \frac{g \gamma_2}{2f} \mathbf{k} \times \text{grad}_h (\mathcal{H})^2, \qquad\qquad (13)$$

where $\mathbf{k}$ indicates a unit vertical vector. Consequently $\mathcal{H}$ is linked to the averaged velocity and defines the streamlines of the mean transport. It is shown below that $\mathcal{H}$ easily allows to define the first baroclinic mode.

Using $\mathcal{H}$, Eq. (6) can then be written

$$\frac{\partial}{\partial t}H(\mathcal{H}, \zeta, f) - \frac{\beta g \gamma_2 \mathcal{H}}{f^2}\frac{\partial \mathcal{H}}{\partial x} = -w_e \qquad (14)$$

or, since by (12) H is an implicit function of $\mathcal{H}, \zeta = f/h_2$, and f, $\partial H/\partial t = (\partial H/\partial \mathcal{H})(\partial \mathcal{H}/\partial t) + (\partial H/\partial \zeta)(\partial \zeta/\partial t)$,

$$\frac{\partial \mathcal{H}^2}{\partial t} - c_1 \frac{\partial \mathcal{H}^2}{\partial x} = -\lambda w_e - \mu \qquad (15)$$

with

$$c_1 = \frac{\beta g \gamma_2 \mathcal{H}}{f^2}\left(\frac{\partial H}{\partial \mathcal{H}}\right)^{-1} = \frac{\beta g}{f^2}(\gamma_1(H - f/\zeta) + \gamma_2 H)$$

$$\lambda = 2\mathcal{H}\left(\frac{\partial H}{\partial \mathcal{H}}\right)^{-1} = 2H + 2\frac{\gamma_1}{\gamma_2}(H - f/\zeta)$$

$$\mu = 2\mathcal{H}\frac{\partial H}{\partial \zeta}\left(\frac{\partial H}{\partial \mathcal{H}}\right)^{-1}\frac{\partial \zeta}{\partial t} = -2f\frac{\gamma_1}{\gamma_2}\frac{H - f/\zeta}{\zeta^2}\frac{\partial \zeta}{\partial t}, \qquad (16)$$

where we have used for convenience $\mathcal{H}^2$ rather than $\mathcal{H}$. Similarly, the potential vorticity equation (8) is written

$$\frac{\partial \zeta}{\partial t} + \frac{\beta g \gamma_2}{f}\left(-\left(\frac{\partial H}{\partial \mathcal{H}}\frac{\partial \mathcal{H}}{\partial f} + \frac{\partial H}{\partial \zeta}\frac{\partial \zeta}{\partial f} + \frac{\partial H}{\partial f}\right)\frac{\partial \zeta}{\partial x}\right.$$

$$\left. + \left(\frac{\partial H}{\partial \mathcal{H}}\frac{\partial \mathcal{H}}{\partial x} + \frac{\partial H}{\partial \zeta}\frac{\partial \zeta}{\partial x}\right)\frac{\partial \zeta}{\partial f}\right) = 0 \qquad (17)$$

or equivalently

$$\frac{\partial \zeta}{\partial t} + c_z\frac{\partial \zeta}{\partial x} + c_m\frac{\partial \zeta}{\partial f} = 0 \qquad (18)$$

with

$$c_z = -\frac{\beta g \gamma_2}{f}\left(\frac{\partial H}{\partial \mathcal{H}}\frac{\partial \mathcal{H}}{\partial f} + \frac{\partial H}{\partial f}\right)$$

$$= -\frac{\beta g \gamma_2}{f(\gamma_1(H - f/\zeta) + \gamma_2 H)}\left(\gamma_2\mathcal{H}\frac{\partial \mathcal{H}}{\partial f} + \gamma_1\frac{H - f/\zeta}{\zeta}\right)$$

$$c_m = \frac{\beta g \gamma_2}{f}\frac{\partial H}{\partial \mathcal{H}}\frac{\partial \mathcal{H}}{\partial x} = \frac{\beta g \gamma_2^2 \mathcal{H}}{f(\gamma_1(H - f/\zeta) + \gamma_2 H)}\frac{\partial \mathcal{H}}{\partial x}.$$

$$(19)$$

The system (6) and (8) is thus replaced by the two coupled nonlinear equations (15) and (18) with unknowns $\mathcal{H}^2$ and ζ,

which are integrated numerically using a method of successive linearizations (see appendix A).

At first, $\mathcal{H}$ increases in all of the basin as was found north of the subduction line, where $\mathcal{H}$ reduces to h_2. This is illustrated in Fig. 4 O=, which represents different stages of $\mathcal{H} - \mathcal{H}_f$, where $\mathcal{H}_f$ denotes $\mathcal{H}$ at the final equilibrium state. The increase in $\mathcal{H}$ occurs rapidly in the southern part of the basin (after 3 yr, $\mathcal{H}$ is in approximate steady state) but more slowly in the northern part, so the variations of $\mathcal{H}$ only becomes negligible throughout the basin after about 12 yr. The dynamics of the system is then only driven by the advection of potential vorticity, as discussed below.

To show that the adjustment of $\mathcal{H}$ is consistent with the travel time of the first-mode baroclinic Rossby wave, we consider a simplified version of (15), where $\partial\mathcal{K}/\partial t$ is neglected and

$$\left(\frac{\partial H}{\partial \mathcal{H}}\right)^{-1} = \frac{\gamma_2 H + \gamma_1 h_1}{\sqrt{\gamma_1 \gamma_2 h_1^2 + \gamma_2^2 H^2}}$$

replaced by its average (noted K) between the initial and the final state, a very good approximation during the first phase of the adjustment. Then, (15) becomes

$$\frac{\partial \mathcal{H}}{\partial t} - c_R \frac{\partial \mathcal{H}}{\partial x} = -Kw_e \quad \text{with } c_R = K\frac{\beta g \gamma_2}{f^2}\mathcal{H}, \quad (20)$$

a nonlinear wave equation forced by Ekman pumping, which can be solved as in section 3. Note that K is always larger than 1, reaching its maximum where h_1 is maximum (in Fig. 4 O=, the maximum is $K = 1.33$).

The solution computed from (20) is very similar to, but smoother than that in Fig. 4 O=, as illustrated at year 3 in Fig. 5 O=. The wave front (dashed line) approximately corresponds to the zero contour in Fig. 4 O=. There are slight differences in the westernmost part of the basin, but neither equation applies close to the recirculation area. Note that the propagation is purely zonal and is independent of the mean geostrophic flow; that is, the non-Doppler shift effect still holds south of the subduction line. Figure 6 O= shows for the final state the phase velocity c_R, which matches (10) at the subduction line and compares well to those given for the first baroclinic mode by Killworth et al. (1997, Fig. 7 O=), reproducing in particular the small tilt of the isocontours (from the southeast to the northwest). This tilt increases with the Ekman pumping, as seen from the expression of c_R and (11)–(12). The phase velocity in the 2.5-layer model is larger than that in a 1.5-layer model of equal depth. The differences are mainly due to our use of $\mathcal{H}$ as basic variable, thereby taking into account the mean baroclinic flow as done in a more complex framework by Killworth et al. (1997). Using $\mathcal{H}$ to define the wave speed corresponds to replacing H by $K\mathcal{H} \simeq (\gamma_2 H + \gamma_1 h_1)/\gamma_2$. The increase in c_R is negligible at the eastern boundary but increases westwards, reaching 50% in the westernmost part of the basin where $h_1 \simeq H/2$. This enhanced phase velocity is qualitatively consistent with the faster speed of the observed Rossby waves (Chelton and Schlax 1996). It is also worth noting that these values differ notably from the Rossby wave celerity introduced by Liu, who used

$$c_R = \frac{\beta g \gamma}{f^2} \frac{h_1(H - h_1)}{H}$$

[hereafter $C_{Liu}(h_1)$]. For $H = 600$ m, and $h_1 = H/4$ (i.e., far from the eastern boundary where $h_1 = 0$), $C_{Liu}(h_1)$ is equal to 0.6 cm s^{-1} at 25°N, seven times smaller than in Fig. 6 O=. It is shown in section 5 that $C_{Liu}(h_1)$ is, in fact, of the order of c_2, the velocity of the second baroclinic mode, the only mode that was represented by Liu.

The evolution of the potential vorticity is more complex as it varies everywhere and only reaches a steady state after several decades (Fig. 7 O=). During the first 12 years, the thermocline depth changes north of the subduction line, altering the potential vorticity of the subducting water as seen in the northern part of the domain at year 1 and 7. At the same time, $\mathcal{H}$ varies south of the subduction line, and the shadow zone, which was at rest, becomes active as found by Liu, but the velocity remains small, resulting in a slight increase in potential vorticity off the southeast corner. After about 12 yr, $\mathcal{H}$ has reached an equilibrium along the subduction line, and consequently the potential vorticity of subducting water no longer varies. It is now advected by the second-layer flow, and by year 20, the basin reaches a new equilibrium north of $f = 8 \times 10^{-5}$ s^{-1}. Farther south, however, more time is needed for equilibrium because of the smallness of velocity in the second layer, and a steady state is only reached after more than 40 years. Note that we have somewhat arbitrarily chosen in the recirculation area to set to zero the zonal gradient of potential vorticity along the western boundary when an eastward

velocity is detected (between 28° and 38°N). This choice, together with a small smoothing by the numerical scheme, causes the final state to differ from the true one (compare year 40 to final state). This drawback will be remedied in section 5.

Figure 8 ⊙ shows how the second-layer depth H reaches its new equilibrium state H_f. In the ventilated area, the main changes occur during the first decade (compare years 1 and 7) and are due to the propagation of the first baroclinic Rossby mode. However, H is also affected by the second mode, and the comparison with Fig. 4 ⊙ shows that H is not as well suited as $\mathcal{H}$ to represent the first baroclinic mode since $\mathcal{H}$ is in equilibrium after 12 yr, while H still varies, although its variations never exceed 30 m in the ventilated area. In the shadow zone, the variations of H do not exceed 40 m and have the same order of magnitude after the propagation of the first baroclinic mode, suggesting that the two baroclinic modes play a comparable role.

The bulk of the adjustment is thus similar to that north of the subduction line and is due to baroclinic processes, not the barotropic ones as in Liu. The increase in Ekman pumping generates a first-mode Rossby wave, which is well described by $\mathcal{H}$ and propagates rapidly across the basin, with large effects in the ventilated area, without being significantly affected by the geostrophic flow and the differences between the ventilated and the shadow zones, except through the variations in layer depth. Consequently, the influence of wind stress changes on the thermocline is again better represented with a one-mode model with a basic state at rest than with a two-layer model with a flat thermocline bottom, although the former only describes how H evolves and underestimates the Rossby wave speed. On the other hand, ζ and the individual layer depths show a more complex behavior and their slower adjustment is also influenced by the second baroclinic mode. To clarify its role, we investigate below the mechanisms of the adjustment after passage of the first mode.

The same gross features are found during spindown, except for the longer adjustment time. The basin is first affected by a first-mode baroclinic Rossby wave that lifts both layers, but with a slightly longer timescale, because of the nonlinearity. It is then controlled by smaller changes associated with the second baroclinic mode, which remains active and expands the shadow zone. In Liu, the appearence of two gyres was emphasized, an anticyclonic one to the north and a weak cyclonic one to the south. However, this phenomenon was not seen in the 2.5-layer model.

5. Mechanisms linked to the second baroclinic mode

To clarify the role of the second baroclinic mode and facilitate the comparison with Liu, we now focus on the potential vorticity adjustment. Since $f\mathbf{k} \times (\rho_1\mathbf{v}_1 - \rho_2\mathbf{v}_2) = -\rho_0 g\gamma_1 \, \mathrm{grad}_h h_1$, h_1 is the the natural variable to investigate the second baroclinic mode. Using the definition of $\mathcal{H}$ to replace ζ in (8) by h_1, the potential vorticity equation can be written

$$\frac{\partial h_1}{\partial t} + \frac{\gamma_2 H}{\gamma_1 h_1 + \gamma_2 H}\mathbf{v}_a \, \mathrm{grad}_h h_1 + \frac{\gamma_2 H}{\gamma_1 h_1 + \gamma_2 H}c_r\frac{\partial h_1}{\partial x}$$

$$= \frac{\gamma_2 \mathcal{H}}{\gamma_1 h_1 + \gamma_2 H}\left(\frac{\partial \mathcal{H}}{\partial t} - \frac{\beta g \gamma_2 h_2}{f^2}\frac{\partial \mathcal{H}}{\partial x}\right) \qquad (21)$$

with

$$c_r = -\frac{\beta g \gamma_1 h_1 h_2}{f^2 H}.$$

This generalizes to the time dependent case the h_1-equation given in the stationary case in Luyten and Stommel (1986) or Cushman-Roisin (1987). Equation (21) shows that h_1 is advected in proportion to the averaged flow $\mathbf{v}_a$ (which only depends on $\mathcal{H}$ and thus the first baroclinic mode) and a westward velocity

$$c_2 = \frac{\gamma_2 H}{\gamma_1 h_1 + \gamma_2 H}c_r,$$

which we associate with the phase speed of the second baroclinic mode. Figure 9 ⊙ shows that the velocity of the front associated to the second baroclinic mode is ten times smaller than that of c_1 in Fig. 6 ⊙. Note that, in this interpretation, the propagation of the second baroclinic mode is strongly affected by the vertically averaged flow, contrasting with the non-Doppler shift of the first mode. The terms on the right hand side represents the local forcing by the Ekman pumping w_e and

the effects of the passage of the first baroclinic mode. An equation for H can be obtained similarly:

$$\frac{\partial H}{\partial t} + \frac{\gamma_2 H}{\gamma_1 h_1 + \gamma_2 H} \mathbf{v}_a \, \text{grad}_h H + \frac{\gamma_2 H}{\gamma_1 h_1 + \gamma_2 H} C_r \frac{\partial H}{\partial x}$$

$$= \frac{\gamma_2 \mathcal{H}}{\gamma_1 h_1 + \gamma_2 H} \frac{\partial \mathcal{H}}{\partial t}. \tag{22}$$

It is similar to (21) except for a simpler forcing term. The characteristics and propagation of the front is thus similar for h_1 and H, hence for h_2.

After $\mathcal{H}$ has reached its equilibrium value, that is, after the first mode adjustment (year 12 in the numerical experiment), we have $\partial \mathcal{H}/\partial t = 0$ and

$$\frac{\beta g \gamma_2 \mathcal{H} \partial \mathcal{H}}{f^2 \quad \partial x} = w_e,$$

so Eqs. (21) and (22) simplify. However, an analytical solution cannot be obtained because of the complex form of the coefficients, which do not separate the part due to the first baroclinic mode $\mathcal{H}$ and that due to the second one. This lack of analytical solution also holds in the steady case, as was noted by Luyten and Stommel (1986) and Cushman-Rosin (1987) who had to use numerical methods.

To obtain an analytical solution, we introduce a function $\theta(x, y, t)$ (with $\theta \in \,]0, \pi/2[$) defined by

$$\tan\theta = \frac{\gamma_1 h_1 + \gamma_2 H}{\sqrt{\gamma_1 \gamma_2 h_2}}, \tag{23}$$

which provides a measure of the ratio of the two active layer thicknesses and allows one to clearly separate the part due to the first mode from that due to the second mode. Indeed, straightforward algebra shows that the layer depths are related to $\mathcal{H}$ and θ by

$$h_1 = -\mathcal{H}\frac{\sin\theta_1}{\cos\theta_1}\sin(\theta + \theta_1), \qquad h_2 = \mathcal{H}\frac{\cos\theta}{\cos\theta_1}, \quad \text{and}$$

$$H = \mathcal{H}\cos(\theta + \theta_1), \tag{24}$$

where $\theta_1 \in \,]-\pi/2, 0[$ is defined by

$$\sin\theta_1 = -\sqrt{\frac{\gamma_2}{\gamma_1 + \gamma_2}}, \qquad \cos\theta_1 = \sqrt{\frac{\gamma_1}{\gamma_1 + \gamma_2}} \tag{25}$$

(in the numerical experiments $\gamma_1 = \gamma_2$, and $\theta_1 = -\pi/4$). Introducing these expressions in (8) leads to

$$\frac{\partial \theta}{\partial t} + (c_x + c_2)\frac{\partial \theta}{\partial x} + c_y\frac{\partial \theta}{\partial y} = p, \tag{26}$$

with

$$c_2 = \frac{\gamma_2 H}{\gamma_1 h_1 + \gamma_2 H} c_r = -\frac{\beta g \gamma_2}{f^2} \frac{\cos\theta \sin(\theta + \theta_1)}{\sin\theta} \mathcal{H}$$

$$p = \frac{\cos\theta}{\sin\theta \mathcal{H}} \left(\frac{\partial \mathcal{H}}{\partial t} - \frac{\beta g \gamma_2}{f^2} \cos(\theta + \theta_1) \mathcal{H} \frac{\partial \mathcal{H}}{\partial x} \right). \qquad (27)$$

If $\mathcal{H}$ is constant, one has

$$p = -\frac{\cos\theta \sin(\theta + \theta_1)}{\sin\theta \mathcal{H}} w_e,$$

$$c_x = \frac{\sin\theta_1 x}{\sin\theta \mathcal{H}} \left(2w_e + f \frac{\partial w_e}{\partial f} \right); \quad \text{and} \quad c_y = \frac{-\sin\theta_1}{\sin\theta \mathcal{H}} \frac{f}{\beta} w_e$$

in (27), which can then be written

$$dt = ds \qquad dx = (c_x + c_2)ds \qquad dy = c_y ds$$

$$d\theta = pds, \qquad\qquad\qquad\qquad (28)$$

where s defines again the abscissa along characteristics. As shown in appendix B, (28) can be solved analytically, thereby improving on the numerical results of section 4. The conditions at $s = 0$ are given in three domains. The initial state is specified in domain $\mathcal{D}_1$, defined by $t = 0$, $x \leqslant 0$, $f \leqslant f_j$, which corresponds to the whole basin south of the subduction line. The conditions imposed by the dynamics north of the subduction line are prescribed at all times in domain $\mathcal{D}_2$, defined by $t \geq 0$, $x \leqslant 0$, $f = f_j$, and those along the eastern boundary in $\mathcal{D}_3$, defined by $t \geq 0$, $x = 0$, $f \leqslant f_j$. Note that the characteristics coming from the subduction line at $t = 0$ and from its intersection with the eastern coast at $t \geq 0$ define the new ventilated zone, whereas those coming from the eastern boundary at $t = 0$ and from its intersection with subduction line at $t \geq 0$ define the new shadow zone (heavy line in Fig. 11 ⊙ and 12 ⊙ below).

Figure 10 ⊙ shows the thickness ratio θ. Note that in the initial (panel a) and final (panel c) state, θ depends only on latitude in the ventilated zone, which would not be the case for h_1 since the latter depends on $\mathcal{H}$, hence on the longitude. However, in the two-layer model of Liu, the first layer depth also depended only on latitude in the ventilated zone since the thermocline bottom was at a constant depth. The initial state for the integration of (28) is taken from the numerical calculation at the beginning of year 13 (panel b). The thermocline depth has increased but the ocean is out of equilibrium. The initial ventilated and shadow zones can still be recognized (compare with panel a), although their boundaries have been smoothed by the numerical scheme and θ depends slightly on longitude in the ventilated zone. The evolution of θ is shown in perspective view in Fig. 11 ⊙ at year 18 and 23 (its evolution ceases after year 28). Each grid element in these panels is the image along a characteristic of an initial rectangle (defined at $s = 0$), hence its distortion reflects the mechanisms at play. The time step chosen in $\mathcal{D}_2$ and $\mathcal{D}_3$ for the integration is equal to 1 yr, so the zonally oriented lines in the new ventilated zone and the meridonally oriented lines in the new shadow zone correspond to years 0 to 5 (panel a) or 0 to 10 (panel b). Since θ depends only slightly on longitude in the northern part of the basin, the term $(c_x + c_2)\partial\theta/\partial x$ in Eq. (28) remains much smaller than $c_y \partial\theta/\partial y$ (it vanishes when the equilibrium state is reached since θ then does not depend on the longitude, as mentioned above). Consequently, zonal advection and Rossby wave propagation remain small, and meridional advection dominates. This is reflected by the marked meridional propagation of the front (heavy line) and the grid elements in the northern part of the old ventilated zone, with only weak zonal changes. Note that θ has reached its steady state in the new ventilated zone after the front has passed. The main balance in the northern part of the basin is thus between meridional advection and local Ekman pumping. This agrees with Liu, but only holds after the first baroclinic mode adjustment. Equatorward the situation is more complex. As the shadow zone is no longer at rest, advection occurs everywhere. Moreover, since θ strongly depends on x, $c_2 \partial\theta/\partial x$ dominates in (26) and the second baroclinic mode is active. This is revealed by the strong zonal displacement of the wave front (heavy line) and the grid elements, and by the stretching of the latter in the eastern part of the old shadow zone. It reflects an approximate balance between Ekman pumping and the second baroclinic mode as well as the latitudinal

dependence of its wave speed. Behind the front originating from the eastern boundary, a new shadow zone is created, which is at rest since H remains constant. Figure 11c shows the depth of the layers at year 17. The different dynamical zones are separated by sharp boundaries since our solution of (26) is not affected by numerical smoothing as in section 4 nor by the recirculation area, which is always delineated by characteristics.

Qualitatively, the thermocline evolution is similar during spindown. The initial state of the integration of (28), taken after 15 yr (Fig. 10d) as the first-mode adjustment, was a little slower (section 4). The thermocline has been lifted by the first baroclinic mode and the averaged velocity $\mathbf{v}_a$ has become smaller [see (13)]. The state of θ at year 20 (panel a) and 30 (panel b) is shown in Fig. 12 , suggesting the same dynamics during spinup:weak Rossby waves in the northern part of the basin and intense wave activity elsewhere. As before, the spindown is much slower than the spinup, as seen by the smaller distance between the zonally oriented lines in the new ventilated zone and between the meridionaly oriented lines in the new shadow zone. The longer adjustment is due to the decrease of the averaged advection in the ventilated zone, as well as that of the second-mode phase velocity in the shadow zone. The evolution of θ only ceases after year 40 instead of 28.

A detailed comparison with Liu is not warranted, but it is easily seen that his analysis remains coarsely valid for the second phase of the adjustment if we associate θ to his first-layer depth and interpret his discussion of the first baroclinic mode as really pertaining to the second (note that c_2 is slightly smaller but otherwise very similar to C_{Liu} and c_r is similar to C_{Liu}). Nonetheless, Liu's assumption of a flat thermocline bottom leads to important differences in the results and interpretation:

1. Although (26) is close to the corresponding equation for the first layer depth in Liu, density advection is by a baroclinic flow and not a barotropic one, with corresponding differences in the associated timescales: its adjustment takes a decade instead of being instantaneous.

2. There is some wave activity in the north because the first baroclinic mode has tilted the lines of constant θ ($c_2 \partial \theta/\partial x \neq 0$).

3. The differences in adjustment time betwen spinup and spindown are larger in the present study since only the second baroclinic mode was represented in Liu, and it had no linear dependence on the effective layer depth, only an indirect one via the first-layer depth.

6. Conclusions

Using a method of successive linearization, we have numerically simulated the spinup of a 2.5-layer model of the ventilated thermocline and interpreted it in terms of baroclinic Rossby wave propagation. The first baroclinic mode was defined in a forced wave equation for an effective depth $\mathcal{H}$, which determined the averaged flow in the two active layers. The second baroclinic mode was defined in an equation for h_1 or for θ, a function of the ratio between the two-layer thickness, which determined the differences in their behavior. Two periods of different dynamics characterize the adjustment. During the first decade, the Ekman pumping change mainly creates a first-mode baroclinic Rossby wave that deepens the thermocline both north and south of the subduction line without being directly affected by the mean flow. However nonlinearities affect the wave propagation and lead to faster phase speed in the 2.5-layer model than in a 1.5-layer one with the largest differences in the western part of the basin where it can reach 50%. Although our study gives some support to the common use of simplified normal mode models (FMZ; Sturges and Hong 1995) that prescribe the first baroclinic mode and assume a basic state at rest, it confirms that more complex models are needed to match the largest phase velocity computed from observed data (Chelton and Schlax 1998).

After crossing of the first-mode wave front, $\mathcal{H}$ is in approximate equilibrium, but not θ south of the subduction line. The dynamics can then be described to a good approximation by the conservation of potential vorticity. In the initial ventilated area, the Ekman pumping is primarily balanced by meridional advection, but zonal advection and the second baroclinic mode are also active, resulting in fairly small depth variations and a slow return to a stationary state. In the initial shadow zone that was set in motion, the main balance is between the second baroclinic mode and Ekman pumping, the advection by the averaged flow having a smaller effect. Although the resulting depth changes are much smaller than during the first stage of the adjustment, these dynamics lead to the establishment of new ventilated and shadow zones. The second phase of the adjustment is thus more complex and involves a second baroclinic mode whose propagation is strongly controlled by the mean meridional advection. It is therefore inadequate to use a baroclinic mode higher than the first one in modal models with a basic state at rest. This explains why Sturges and Hong (1995) found that adding the second baroclinic mode brought no improvement to their sea-level prediction.

The main difference between spinup and spindown is that the latter takes longer. During the first stage of the adjustment, the nonlinearities slow the propagation of the first baroclinic mode. During the second, the celerity of the second mode and

the averaged velocity of the flow are decreased because the thermocline has become shallower and w_e is weaker. Such a dissymmetry between the two cases should affect the oceanic response to harmonic and stochastic variations in the Ekman pumping.

Our results strongly differ from those of Liu who, by assuming that the thermocline bottom remains flat, filtered out the first baroclinic mode, which actually largely dominates the adjustment. Nonetheless, much of Liu's analysis remains valid, albeit in a simplified setting, for the second stage of the adjustment allowed one to interpret his first baroclinic mode as the second one and his initial barotropic adjustment as the 10-yr long baroclinic one. On the other hand, the dominant role of the first baroclinic mode and the strong influence of advection on the second mode that is demonstrated here are consistent with the recent analysis of Huang and Pedlosky (1999) (provided that what they call barotropic response is understood as the first baroclinic mode) who compared the steady-state response of a 2.5-layer model to different forcing fields, with that of Liu (1999) who used the WKB approximation to study a Rossby wave in a 2.5-layer quasigeostrophic model, and with the numerical simulations of Nakamura (1998). Finally, our results are consistent with recent observational evidence. Indeed, Deser et al. (1999) showed that the first baroclinic mode response to changes in the Ekman pumping largely explains the observed variability of the Kuroshio. They also observed a midbasin temperature anomaly that was slowly moving southward, then westward, as predicted by the trajectories associated to our second baroclinic mode.

REFERENCES

Anderson, D. L. T., and P. D. Killworth, 1979: Non-linear propagation of long Rossby waves. *Deep-Sea Res.,* **26A,** 1033–1050..

Chelton, D. B., and M. G. Schlax, 1996: Global observations of oceanic Rossby waves. *Science,* **272,** 234–238..

Cushman-Roisin, B., 1987: On the role of heat flux in the Gulf Stream–Sargasso Sea subtropical gyre system. *J. Phys. Oceanogr.,* **17,** 2189–2202.. Find this article online

Deser, C., M. A. Alexander, and M. S. Timlin, 1999: Evidence for a wind-driven intensification of the Kuroshio current extension from the 1970s to the 1980s. *J. Climate,* **12,** 1697–1706.. Find this article online

Euvrard, J., 1985: *Méthodes Numériques.* Masson, 256 pp..

Frankignoul, C., 1981: Low-frequency temperature fluctuations off Bermuda. *J. Geophys. Res.,* **86,** 6522–6528..

—— ,P. Müller, and E. Zorita, 1997: A simple model of the decadal response of the ocean to stochastic wind stress forcing. *J. Phys. Oceanogr.,* **27,** 1533–1546.. Find this article online

Huang, R. X., and J. Pedlosky, 1999: Climate variability inferred from a layered model of the ventilated thermocline. *J. Phys. Oceanogr.,* **29,** 779–790.. Find this article online

Joyce, T. M., and P. Robbins, 1996: The long-term hydrographic record at Bermuda. *J. Phys. Oceanogr.,* **26,** 3121–3131.. Find this article online

Killworth, P. D., D. B. Chelton, and R. A. de Szoeke, 1997: The speed of observed and theoretical long extratropical planetary waves. *J. Phys. Oceanogr.,* **27,** 1946–1966.. Find this article online

Latif, M., and T. P. Barnett, 1994: Causes of decadal climate variability in the North Pacific/North American sector. *Science,* **266,** 96–99..

Liu, Z., 1993: Thermocline forced by varying Ekman pumping. Part I: Spinup and spindown. *J. Phys. Oceanogr.,* **23,** 2505–2522.. Find this article online

—— ,1996: Thermocline variability in different dynamic regions. *J. Phys. Oceanogr.,* **26,** 1633–1645.. Find this article online

—— ,1999: Forced planetary wave response in a thermocline gyre. *J. Phys. Oceanogr.,* **29,** 1036–1055.. Find this article online

—— ,and J. Pedlosky, 1994: Thermocline forced by annual and decadal surface temperature variations. *J. Phys. Oceanogr.,* **24,** 587–608.. Find this article online

Luyten, J. R., and H. Stommel, 1986: Gyres driven by combined wind and buoancy flux. *J. Phys. Oceanogr.,* **16,** 1551–1560.. Find this article online

— ,J. Pedlosky, and H. Stommel, 1983: The ventilated thermocline. *J. Phys. Oceanogr.,* **13,** 292–309.. Find this article online

Nakamura, H., 1998: Simple model prediction of horizontal temperature fields in the subtropical-subpolar system caused by a sudden change in wind stress curl. *J. Phys. Oceanogr.,* **28,** 1578–1597.. Find this article online

Rhines, P. B., and W. R. Young, 1982: Homogenization of potential vorticity in planetary gyres. *J. Fluid. Mech.,* **122,** 347–367..

Sturges, W., and B. G. Hong, 1995: Wind forcing of the Atlantic thermocline along 32°N at low frequencies. *J. Phys. Oceanogr.,* **25,** 1706–1715.. Find this article online

— ,— ,and A. J. Clarke, 1998: Decadal wind forcing of the north Atlantic subtropical gyre. *J. Phys. Oceanogr.,* **28,** 659–668.. Find this article online

Zorita, E., and C. Frankignoul, 1997: Modes of the North Atlantic decadal variability in the ECHAM1/LSG coupled ocean–atmosphere general circulation model. *J. Climate,* **10,** 183–200.. Find this article online

---

APPENDIX A

7. Numerical Technique

The system (14) and (17) with unknowns $\mathcal{H}^2$ and ζ is integrated numerically using a method of successive linearizations. Between t_n and t_{n+1} where $t_n = n\delta t$, n integer, we linearize the two equations on a prescribed spatial grid around the values reached at time t_n. Then we use the method of characteristics to predict the values at t_{n+1}. As discussed below, the method is accurate to first order in δt and converges for small enough δt, although the spatial interpolations needed at each time step introduce some smoothing near the frontal zones.

To linearize (14) at time t_n around a grid point (x_σ, f_σ), we replace c_1, λ, and μ by their values $c_1(n, \sigma)$, $\lambda(n, \sigma)$, and $\mu(n, \sigma)$, where (n, σ) refer to $(t_n, x_\sigma, f_\sigma)$, which depend on the value of $\mathcal{H}$ and ζ at the same time and location, respectively $\mathcal{H}(n, \sigma)$ and $\zeta(n, \sigma)$. This leads to the equation

$$\frac{\partial \mathcal{H}^2}{\partial t} - c_1(n, \sigma)\frac{\partial \mathcal{H}^2}{\partial x} = -\lambda(n, \sigma)w_e - \mu(n, \sigma), \quad (A1)$$

whose characteristics are given by the system:

$$\frac{dt}{ds} = 1 \qquad \frac{dx}{ds} = -c_1(n, \sigma)$$

$$\frac{d\mathcal{H}^2}{ds} = -\lambda(n, \sigma)w_e - \beta(n, \sigma). \qquad (A2)$$

Integrating the ratio between the first two equations leads to $x - x_\sigma = -c_1(n, \sigma)\delta t$. This last step neglects the x dependence of $c_1(n, \sigma)$ and so remains accurate only if δt is small enough for $x - x_\sigma$ to be smaller than the grid size. The characteristics associated with (14) are thus straight lines given by

$$x = -c_1(n, \sigma)\delta t + x_\sigma \quad \text{and} \quad f = f_\sigma.(A3)$$

Similarly, the ratio between the last two equations in (A2) leads to

$$\frac{d\mathcal{H}^2}{dx} = \frac{2f^2}{\gamma_2\beta g}w_e + \frac{\mu(n, \sigma)}{c_1(n, \sigma)}, \qquad (A4)$$

where we have used (15), which is integrated into

$$\mathcal{H}^2 = \mathcal{H}^2(n, \sigma) + \frac{2f^2 w_e}{\gamma_2 \beta g}(x - x_\sigma)$$

$$+ \frac{\mu(n, \sigma)}{c_1(n, \sigma)}(x - x_\sigma). \tag{A5}$$

This defines $\mathcal{H}$ along the characteristics (A3), leading after interpolation along $f = f_\sigma$ to $\mathcal{H}(n + 1, \sigma)$. Note that when $\partial \mathcal{H} / \partial t$ becomes negligible, μ tends to 0 and the computation of $\mathcal{H}$ becomes exact [compare (A5) with (11)–(12)], insuring convergence to the true value of $\mathcal{H}$. The potential vorticity equation 17 is integrated similarly except that f acts as a variable, and no forcing is applied. The characteristic originating at t_n from (x_σ, f_σ) is the straight line defined by

$$x = c_z(n, \sigma)\delta t + x_\sigma \quad \text{and} \quad f = c_m(n, \sigma)\delta t + f_\sigma, \tag{A6}$$

and the potential vorticity is conserved along it:

$$\zeta(x, y) = \zeta(n, \sigma). \tag{A7}$$

An interpolation (inverse distance method) provides $\zeta(n + 1, \sigma)$. For the characteristics originating from the eastern boundary, one has $h = H_0 = \mathcal{H}$, while for those originating at subduction line $y = y_1$, section 3 yields $\mathcal{H} = H = h_2$. Note however that the recirculation zone on the western side is not correctly represented by the model dynamics.

The potential vorticity gradient in the area that separates shadow and ventilated zones is very sharp and can only be well represented on a grid with high zonal and meridional resolution. Since our algorithm is only accurate to first order in δx, we improved it by using the technique of "extrapolation à la limite" (Euvrard 1985), where a second integration is done on a grid twice finer than the first one. If V_1 denotes a variable computed on the original grid and V_2 the same variable computed on the finer grid, we use $V = 2 \times V_2 - V_1$, accurate to second order in δx. For each integration, the time step δt must be chosen such as $\upsilon \delta t < \delta l$, where υ is the largest velocity involved in the problem and δl the distance between two grid points (CFL condition). The spatial grid is thus a compromise between prohibitive computational cost and coarse resolution. We chose for the finest grid a meridional resolution of 50 km and a zonal one of 150 km. A typical meridional velocity is 0.5 cm s^{-1}, requiring a time step of at most four months. The largest zonal velocity is that associated with a Rossby wave in the southern part of the basin, 14 cm s^{-1}, requiring a time step of at most 10 days, which was chosen. Nonetheless, the new stationary state reached after integration is not identical to the true one because of the interpolation errors in the potential vorticity field.

APPENDIX B

8. Analytical Solution of (28)

The ratio between dy and $d\theta$ in (28) leads to $\sin\theta_1 f\, d\theta = \beta \cos\theta \cos(\theta + \theta_1)\, dy$, which can be written $f\, d\theta = \cos^2\theta \cot\theta_1\, df - \cos\theta \sin\theta\, df$ and integrated into

$$f \tan\theta = f_\sigma \tan\theta_\sigma - (f_\sigma - f) \cot\theta_1, \tag{B1}$$

where $f_\sigma = f_0 + \beta y_\sigma$ and σ refers to conditions at $s = 0$ as previously. The ratio between dx and dy in (28) leads to

$$\frac{d}{dy}(f^2 x w_e) = \frac{\beta}{f \sin\theta_1}[\sin\theta_1 + \sin(2\theta + \theta_1)]$$

$$\times (f^2 x w_e + \gamma_2 \beta g H_0^2/2) \tag{B2}$$

or equivalently

$$\frac{d}{dy}\ln(D^2 + H_0^2)$$

$$= \frac{\beta}{f\,\sin\theta_1}[\sin\theta_1 + \sin(2\theta + \theta_1)] \qquad (B3)$$

with $D^2 = 2f^2 x w_e/(\gamma_2 \beta g)$. The right-hand side only depends on y and can be easily integrated, leading to

$$\frac{\mathcal{H}^2}{(f^2 + (f_\sigma\tan\theta_\sigma + (f_\sigma - f)\cot\theta_1)^2)}$$

$$= \frac{\mathcal{H}_\sigma^2}{(f_\sigma^2 + (f_\sigma\tan\theta_\sigma)^2)}, \qquad (B4)$$

or using (A8) and (23)

$$h_2/f = h_{2,\sigma}/f_\sigma. (B5)$$

Potential vorticity in the second layer is thus conserved along the streamlines in the $(x,\ y)$ space (Lagrangian conservation). There is another interpretation: multiplying (A12) by $f(1 - \tan\theta_1\tan\theta) = f_\sigma(1 - \tan\theta_1\tan\theta_\sigma)$ and using (23), we obtain $H = H_\sigma$. Thus, (A8) and (A11) define the lines of constant H, that is, the direction of the second-layer flow.

From (28), the ratio dt/dy is equal to

$$dt = -\frac{\beta\,\sin\theta\mathcal{H}}{\sin\theta_1\,fw_e}dy \qquad (B6)$$

or, using (A8) and (A11),

$$dt = -\frac{\beta}{\sin\theta_1}[f_\sigma\tan\theta_\sigma + (f_\sigma - f)\sqrt{\gamma_1/\gamma_2}]$$

$$\times \frac{\sqrt{D_\sigma^2 + H_0^2}}{fw_e(y)\sqrt{f_\sigma^2 + (f_\sigma\tan\theta_\sigma)^2}}dy. \qquad (B7)$$

Replacing $w_e(y)$ by its value $w_e = \alpha(f - f_S)(f_N - f)$, and integrating the function

$$[f_\sigma\tan\theta_\sigma + (f_\sigma - f)\sqrt{\gamma_1/\gamma_2}]/fw_e(y)$$

with the condition at $s = 0$ leads to

$$t - t_i = -\frac{1}{\alpha\,\sin\theta_1}\frac{\mathcal{H}_\sigma\cos\theta_\sigma}{f_\sigma}$$

$$\times \left(A\ln\frac{f}{f_\sigma} + B\ln\frac{f - f_S}{f_\sigma - f_S} - C\ln\frac{f_N - f}{f_N - f_\sigma}\right)$$

$$(B8)$$

with

$$A = \frac{f_\sigma \tan\theta_\sigma + f_\sigma\sqrt{\gamma_2/\gamma_1}}{-f_s f_N},$$

$$B = \frac{f_\sigma \tan\theta_\sigma + (f_\sigma - f_s)\sqrt{\gamma_2/\gamma_1}}{f_s(f_N - f_s)},$$

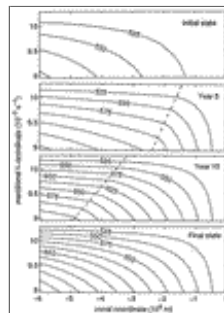$$C = \frac{f_\sigma \tan\theta_i + (f_\sigma - f_N)\sqrt{\gamma_2/\gamma_1}}{f_N(f_N - f_s)}.$$

The characteristics of (28) are computed from (B1), (B4), and (B8).


Figures
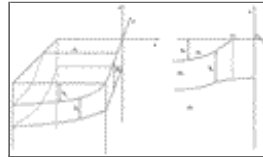
Click on thumbnail for full-sized image.

Fig. 1. Geometry of the 2.5-layer model. The basin is bounded to the east at $x = 0$ and to the north at $y = y_N$. The subduction line is at latitude $y_1(x)$. Left: Perspective view. Right: meridional plane view.

Click on thumbnail for full-sized image.

Fig. 2. Thermocline depth H (in m) north of the subduction line during spinup, at, from top to bottom, year 0, 5, 10, and the final state. The lines of equal depth define the streamlines of the flow and dotted line, the wave front.
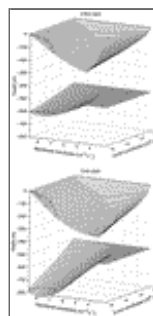
Click on thumbnail for full-sized image.

Fig. 3. Perspective view of the depth of the two active layers in the initial (top) and final (bottom) states of the ocean in the spinup experiment, south of the subduction line. The area where H is constant corresponds to the shadow zone and the area inside the dashed line to the recirculation zone.
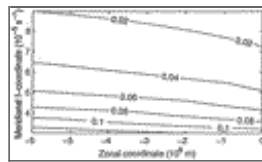
Fig. 4. Differences (in m) between $\mathcal{H}$ and $\mathcal{H}_f$ at year 1, 3, 7, and 20 during spinup.
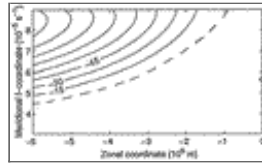
Fig. 5. Map of $\mathcal{H} - \mathcal{H}_f$ (in m) at year 3, neglecting the influence of the temporal variations of the potential vorticity.
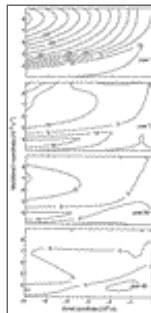
Fig. 6. Wave celerity (in m s^{-1}) of the first baroclinic mode for the final state.
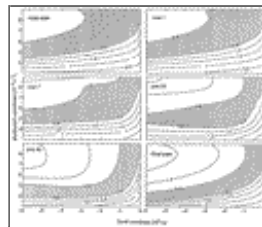
Fig. 7. Potential vorticity in the second layer (in 10^7 m^{-1} s^{-1}) for, from top to bottom, the initial state, year 1, 7, 20, 40, and the final state.

Fig. 8. Differences between H and H_f for, from top to bottom, year 1, 7, 20, and 40 during spinup.
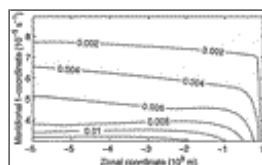
Fig. 9. Wave celerity (in m s^{-1}) of the second baroclinic mode for the final state.

Click on thumbnail for full-sized image.

Fig. 10. Isocontours of θ (in radians) for (a) the initial state, (b) year 12 of the spinup, (c) the final state, and (d) year 15 of the spindown.
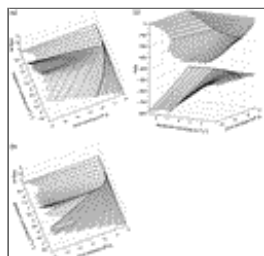
Click on thumbnail for full-sized image.

Fig. 11. Spinup of the ocean during the second part of the adjustment. Perspective view of θ at (a) year 17 and (b) year 22, and (c) of the depth of the two layers at year 17.
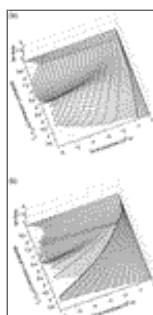
Click on thumbnail for full-sized image.

Fig. 12. Spindown of the ocean during the second part of the adjustment. Perspective view of θ at (a) year 20 and (b) year 30.

Corresponding author address: Dr. Jérôme Sirven, Laboratoire d'Océanographie Dynamique et de Climatologie, Université Pierre et Marie Curie, Tour 14, Étage 2, CC 100, 4 Place Jussieu, 75252 Paris, Cedex 05, France.

E-mail: js@lodyc.jussieu.fr